Appeared in INT. J. REMOTE SENSING, 1997, vol.18, no.13, 2785-2813

Cloud detection and derivation of cloud properties from POLDER

J.C. BURIEZ, C. VANBAUCE, F. PAROL, P. GOLOUB,
M. HERMAN, B. BONNEL, Y. FOUQUART
Laboratoire d'Optique AtmosphÈrique,
UniversitÈ des Sciences et Technologies de Lille, 59655 Villeneuve d'Ascq, France

P. COUVERT
Laboratoire de ModÈlisation du Climat et de l'Environnement,
Centre d'Etudes de Saclay, 91191 Gif-sur-Yvette, France

and G. SEZE
Laboratoire de MÈtÈorologie Dynamique, Ecole Normale SupÈrieure,
75231 Paris, France

(Received 25 July 1996; in final form 25 November 1996)

Abstract . POLDER (POLarization and Directionality of the Earth's Reflectances) is a new instrument devoted to the global observation of the polarization and directionality of solar radiation reflected by the Earth surface-atmosphere system. This radiometer has been on board the Japanese ADEOS platform since August 1996. This paper describes the main algorithms of the POLDER "Earth radiation budget (ERB) & clouds " processing line used to derive products on a routine basis in the early phase of the mission. In addition to the bidirectional reflectance and polarization distribution functions, the main products will be the cloud optical thickness, pressure (from two different methods) and thermodynamic phase. Airborne POLDER observations support the present algorithms for the cloud detection and the derivation of cloud properties.

1. Introduction

In the near future, the Earth will be confronted with the potential risk of rapid environmental changes mainly generated by human activity. The magnitude, regional and temporal distribution of global change should have an important impact on the society, but today, it is not possible to provide answers to questions about these probable effects, mainly due to a misreading of the interdependent processes that affect regional as well as global climate. Among the problems that have received increased attention in recent years are the changes in cloud radiative effects due to greenhouse warming and increase in anthropogenic aerosols.

The most comprehensive way to predict climate change due to an increase of greenhouse gases and aerosols is by means of general circulation models (GCMs). However, current models project sea-surface temperature increases due to a given climate forcing that differ by over a factor of two or three (Cess *et al.* 1990). Such differences can be obtained from an individual GCM by changes only in the cloud parameterization (Senior and Mitchell 1993). This clearly shows the need of realistic representation of clouds in GCMs. Global observations of cloud properties and global measurements of the effect of clouds on radiation are essential to achieve this objective, even if field experiments and surface measurements remain essential to support the satellite measurements at the global scale.

Before the end of the century, a series of satellites will carry several advanced, well-calibrated, instruments designed to provide Earth observations (Wielicki *et al.* 1995). Among them, POLDER (POLarization and Directionality of the Earth's Reflectances) has been launched on the Japanese ADvanced Earth Observing Satellite (ADEOS). Due to its multi-spectral, multi-directional and multi-polarization capabilities, this new radiometer will give useful information on clouds and on their influence on radiation in the short-wave (SW) range.

A first issue concerns the modeling of cloud radiative properties. Clouds are often treated as homogeneous plane-parallel layers composed of spherical particles in the modeling of their effects on climate in GCMs as well as in the derivation of cloud properties from satellite radiances. This approach may be a major weakness in the assessment of the effects of clouds on radiation. For instance, Parol *et al.* (1994a) and Brogniez *et al.* (1992) report errors in SW cloud forcing estimates that might be as large as 40 Wm^{-2} when the morphology of convective clouds or the particle shape in cirrus clouds is neglected. However, presently, it is hardly possible to infer the actual global effect of cloud morphology, i.e. 3D cloud structures, on radiation because from usual scanner radiometers, a given geographic target is observed from an unique direction during a satellite overpass. That means that it is always possible to find a cloud model that satisfies the unique radiance observation. POLDER will provide ~14 quasi-simultaneous radiance measurements of any cloud scene, allowing to check different cloud models and to verify if one of them fulfills the complete set of observations. Such comparisons have already been carried out from airborne POLDER observations (Descloitres *et al.* 1994, 1995).

The matter of the spherical particle hypothesis is mainly related to the treatment of interactions between cirrus clouds and radiation. Up to now, there is few information on cloud microphysics at global scale, except the effective radius of water droplets in low-level clouds (Han *et al.* 1994). The original features of the POLDER sensor will allow to obtain some information on cloud phase and even potentially on the size/shape of cloud particles. Indeed, data acquired using the airborne version of POLDER have shown that the Bidirectional Polarization Distribution Function (BPDF) is a useful tool to detect the presence of liquid particles (Goloub *et al.* 1994).

Another point of interest for improving our understanding of climate changes concerns the Earth Radiation Budget (ERB) measurements. The most advanced procedure to derive the SW flux from the radiance measured in a given direction from ERB scanners has been developed for the ERBE experiment. The estimates of instantaneous reflected fluxes at the pixel scale are obtained by applying bidirectional models derived from a limited set of Nimbus7/ERB scanner measurements (61 days) (Suttles *et al.* 1988). However, the uncertainty related to the use of these bidirectional models limits drastically the accuracy of the estimated fluxes in the short-wave range. Indeed, from ERBS/NOAA-9 intercomparisons, uncertainties of ± 15 Wm^{-2} are expected in the short-wave, on instantaneous observations of $(2.5°)^2$ regions, i.e. 7-8% for a typical reflected flux of 200 Wm^{-2}, to be compared to only 2-3% for radiance measurements (Barkstrom *et al.* 1990). In the same way, comparisons between the Nimbus7-derived radiation field anisotropy and the ERBS-observed anisotropy conclude to an instantaneous r.m.s. error ranging between 4% and 15% due to the use of incorrect bidirectional models (Baldwin and Coakley 1991).

POLDER provides quasi-simultaneous multidirectional radiance measurements (~14 viewing angles) of any scene, that means to observe a part of the Bidirectional Reflectance Distribution Function (BRDF) of the scene. Thus, POLDER could improve the SW flux derivation from ERB scanner measurements, both on a statistical basis, by permitting the construction of new bidirectional models for various surfaces, cloud types and cloud amounts, and, even more interestingly, on an instantaneous basis providing that POLDER and an ERB scanner be aboard the same platform in the future.

As outlined by Wielicki *et al*. (1995), POLDER is part of a series of new sensors that may provide key information for improving our knowledge of clouds, radiation and climate interactions. As a component of the POLDER project, the aim of this paper is to present the algorithms that will be operationally used to derive "ERB & clouds" products (such as cloud cover, cloud pressure, etc...) from ADEOS/POLDER data. These products will be distributed by CNES (Centre National d'Etudes Spatiales, France) from the end of 1997. An overview of the algorithms and products is reported in section 2. Following the methodology applied in the ISCCP scheme (International Satellite Cloud Climatology Project ; Rossow and Schiffer 1991) the cloud analysis based on POLDER measurements is separated into the cloud detection phase and the cloud properties derivation phase. The main algorithms for the cloud detection and the determination of cloud properties, that are supported by airborne POLDER observations, are presented in section 3 and 4 respectively.

2. POLDER "ERB & clouds" processing line

The POLDER instrument on ADEOS is extensively described in Deschamps *et al.* (1994). It consists of a charged coupled device (CCD) matrix detector, a rotating filter wheel carrying the polarizers and filters, and a wide field of view (FOV) telecentric optics. The CCD array is composed of 242 x 274 independent sensitive areas. It corresponds to along-track and cross-track FOVs of ± 43º and ± 51º respectively, and to a diagonal FOV of ± 57º. As the heliosynchronous ADEOS satellite is orbiting at 796 km altitude, the POLDER cross-track swath is about 2200 km and the pixel foot-print is about 6 x 7 km^2 at nadir. The equatorial crossing time is 10:30. As the satellite passes over a target, ~14 different images are acquired in each spectral band which characteristics are reported in table 1.

The POLDER level 1 product will include calibrated reflectances and Stokes parameters projected on a reference Earth equal-area grid at 6.2 km resolution. The level 2 and 3 processings will be split in three lines according to the three thematic interests of POLDER, namely : "ERB, water vapor and clouds", "Ocean color and aerosols over the ocean", "Land surfaces and aerosols over land".

The development of the "ERB & clouds" processing line has two aims : (1) to derive cloud parameters such as cloud optical thickness, cloud pressure and cloud phase and the atmospheric water vapor content ; (2) to provide the necessary data to construct BRDFs (and BPDFs) according to user's own criteria which may be selected afterwards (for instance, cloud cover, cloud pressure, meteorological conditions, etc.). As outlined in the previous section, this second item is important in view of the high remaining uncertainty when inverting radiances to fluxes, simply due to the use of limited and sometimes incorrect bidirectional models.

All the retrieved "ERB & clouds" parameters are based on simple algorithms in order to be produced on a routine basis after a reasonably short validation period. For instance, cloud optical thickness is derived by using a radiative transfer model based on the plane-parallel approximation. That does not take full advantage of the POLDER capability to observe the radiation field anisotropy. Thus more complex algorithms should be developed in the future. Nevertheless, the present product should already allow to check the validity of the usual plane-parallel model on a global basis.

As above-mentioned, POLDER offers special capabilities but a limited data sampling because of the sun-synchronous orbit of ADEOS. Another limitation, which is a constraint mainly for the "ERB & clouds" line, is due to the geographic relocalization of the POLDER pixels which does not take into account the cloud altitude. By considering the 14 view angles for each pixel this induces an horizontal shift in the registration that varies from $\sim \pm 0.1$ pixel for stratus up to $\sim \pm 2$ pixels for cirrus. Because of this shift, a pixel may present different properties according to the direction of the satellite observation. Consequently, calculations are made independently for every pixel and for every direction. Then, in order to minimize the horizontal shift effect, the results are averaged over a "super-pixel" composed of typically 9 x 9 geographic pixels. That presents the advantage of a reduced data flow. However, in order to preserve some information about spatial heterogeneity, standard deviations are calculated. Precisely, a super-pixel corresponds to a 0.5^o x 0.5^o area at the equator, that will made POLDER products easily comparable to ISCCP ones which scale is 2.5^o x 2.5^o (Rossow and Schiffer 1991). The resolution of a super-pixel appears also adequate for BRDF studies because it is about $(50\ km)^2$ and then close to the spatial resolution of typical ERB scanners. Note that although one of the objectives of the POLDER mission is to construct new bidirectional models, only BRDFs corresponding to scene types defined in the context of ERBE (Suttles *et al.* 1988) are routinely produced. Our choice has been to leave the selection open for additional criteria according to which new classifications of the BRDFs will have to be made. The POLDER "ERB & clouds" line thus provides the data necessary to construct these new BRDFs (and BPDFs) according to user's own criteria.

The "ERB & clouds" level 2 and 3 products are detailed in tables 2 and 3 respectively. The chart of POLDER "ERB & clouds" processing is reported in figure†1. The description of the first algorithm, that concerns correction for gaseous absorption and stratospheric aerosol effect, is reported in appendix. The algorithms for cloud detection and the derivation of cloud properties are described in the next sections. The algorithm for precipitable water content is described in Leroy *et al.* (1996).

3. Cloud detection scheme

3.1. *POLDER data*

As ADEOS was launched in August 1996, we had not satellite data at our disposal during the preliminary phase of the POLDER mission. However, our algorithms have been made from the experience acquired by analyzing a lot of measurements performed by the airborne simulator of POLDER during several international field experiments (for instance ASTEX/SOFIA, Weill *et al*. 1996 ; EUCREX'94, Descloitres

et al. 1995). The greater part of POLDER measurements dedicated to the study of clouds has been performed using spectral filters that are very similar to those mounted in the spaceborne version of the instrument but has been acquired mainly over the ocean (for instance off the coast of Brittany in the case of the EUCREX'94 campaign). In our operational processing line, the treatment of POLDER data is divided into two classes of geographic pixels labeled namely "ocean" and "land". While the body of the overall algorithm is the same, the different thresholds used either in the cloud detection scheme or in the derivation of cloud properties are adapted depending on the scene type, i.e. depending on the geographic location of the POLDER pixel.

In this paper, in order to illustrate the working and/or the results of the different algorithms running in the "ERB & clouds" line, we mainly utilize some sets of POLDER images acquired during the EUCREX'94 campaign. Figure 2 shows typical features of bidirectional measurements performed by the POLDER instrument aboard the German FALCON aircraft during this campaign. The three sets of images correspond to acquisitions over clear ocean, stratocumulus and cirrus respectively (table 4). From lidar measurements made in the vicinity of the FALCON, the stratocumulus cloud top was at 1.0 ± 0.1 km and the cirrus cloud top varied from 6 to 10 km.

For each scene type, figure 2 displays instantaneous images that represent (a) the ratio of reflectances measured in the narrow and the wide channels centered at 763 and 765 nm, R_{763}/R_{765} , (b) the reflectance measured at 865 nm, R_{865} and (c, d) the polarized reflectances measured at 443 and 865 nm, PR_{443} and PR_{865} respectively. Useful information about viewing directions is reported in (e) : the expected region of the solar specular reflection (within a cone of half-angle of 30°), the expected cloud-bow region (scattering angle γ between 135° and 150°) and the expected region of maximum molecular polarization ($80° < \gamma < 120°$). Note that the sun zenith angle was close to 40° for the three pictures but the aircraft direction relative to the sun was different from one another. All this information is used either for detecting cloudy pixels or for inferring cloud properties over ocean as illustrated in the following.

Airborne POLDER images presented in figure 2 correspond to an area of about $(5\ km)^2$ and are composed of pixels with footprint of about $(20\ m)^2$. As above-mentioned, the main difference between POLDER and an usual scanning radiometer is its capability to provide instantaneously the BRDF of an observed scene as long as it is homogeneous, at the scale of $(5\ km)^2$ in the present case. This is clearly highlighted on the "clear-ocean" pictures where the glitter phenomenon is quite recognizable. For the stratocumulus cloud, the rainbow phenomenon which is characteristic of liquid water droplets markedly appears in the polarization images while it is not discernible in the unpolarized reflectance image because of cloud heterogeneity. Single and low-order scattering that occurs near the cloud top results in polarized reflectance, but the effects of this polarization are washed out by multiple scattering, deeper in the cloud. Consequently, the fraction of polarized light scattered by the cloud does not depend on the cloud optical thickness as soon as it is larger than about 2 (Goloub *et al.* 1994). Therefore the polarized signal, unlike the unpolarized one, is few sensitive to spatial variability of the cloud optical thickness, i.e. to cloud heterogeneity. On the third set of pictures, the cirrus cloud appears rather flat, that points out both a weak

heterogeneity of the cloud structure and a weak anisotropy of the reflected light.

3.2. *Overview of the algorithm*

Most cloud detection algorithms use both visible reflectance and brightness temperature (e. g. , the review in Rossow *et al.* 1989). Indeed, these two quantities are mainly sensitive respectively to the visible cloud optical thickness and to the cloud altitude, which are the most important cloud parameters with respect to cloud-radiation interactions. Here, the spectral range of the POLDER instrument is restricted to visible and near-infrared wavelengths. However, the two spectral channels centered on the oxygen A band allow the derivation of an "apparent pressure" which represents roughly the cloud pressure as the brightness temperature represents roughly the cloud top temperature. Moreover, additional information about cloud location within the atmosphere can be obtained from polarization measurements.

The POLDER cloud detection algorithm is based on a series of sequential tests applied to each individual pixel. The first step concerns every viewing direction (figure 3). Four tests aim at detecting clouds while two additional ones are used to identify cloud-free pixels. Pixels that do not satisfy any of these six tests are labeled undetermined. After this series of tests, each individual pixel is thus labeled as clear, cloudy or undetermined for a given viewing direction. Note that, particularly for cloud edges, a pixel may appear as cloudy in a direction and clear in another one. A second series of tests is performed by using the multi-directional and the spatial information to re-examine the undetermined pixels.

The tests are detailed in the following and discussed with the help of the data acquired with the airborne version of the instrument. The threshold values used in these tests are only indicative. They will be adjusted after the launch of ADEOS.

3.3. *Apparent pressure test*

The first test is a pressure threshold one, using mainly the R_{763}/R_{765} ratio as indicative of the cloud contamination.

The use of atmospheric absorption in the oxygen A band to infer cloud pressure has been suggested by several authors (e.g. Yamamoto and Yark 1961, Chapman 1962) . Since then, some theoretical efforts (Fisher and Grassl 1991, O'Brien and Mitchell 1992) and aircraft measurements (Fisher *et al.* 1991, Parol *et al.* 1994b) have been carried out. All these studies have shown that the oxygen A band is potentially efficient for determining the cloud-top pressure. They also showed that the main difficulty lies in the photon penetration problem and the influence of ground reflectivity. However, in this first step, all scattering effects are neglected and the atmosphere is assumed to behave as a pure absorbing medium overlying a perfect reflector located at pressure P_{app}. This "apparent" pressure is related to the oxygen transmission T_{O2} that is derived from the R_{763}/R_{765} ratio (see Appendix). Practically, P_{app} is calculated from a polynomial function of T_{O2} and the air-mass factor m . The coefficients of the polynomial are fitted from line-by-line simulations.

Figure 4 shows the histograms of P_{app} for the three selected scenes of figure 2. The apparent pressure is close to 350 hPa and 900 hPa for the cirrus and the stratocumulus cloud respectively. These values agree with the cloud pressure values

expected from lidar measurements. On the contrary, for the clear-ocean case, P_{app} ranges from 650 to 1200 hPa while the sea-surface pressure was 1008 hPa. This large scatter of values of P_{app} is due to the low value of the sea-surface reflectance outside of the sun-glint region. Indeed, when the measured reflectance values are very low, the radiometric noise induces a very large error on P_{app} . In addition, the part of the reflected light due to molecules and aerosols is then no more negligible, that can induce a slight bias on the apparent pressure. When only the highest values of reflectance are preserved for the clear-ocean case, the values of P_{app} tend towards the sea-surface pressure.

Using a crude threshold on P_{app} would allow to identify as cloudy only the pixels for which the apparent pressure is lower than about 600 hPa (see figure 4). Consequently, a simple correction is made by adding to P_{app} a term ΔP which is inversely proportional to the reflectance. Practically, from simulations, we established :

$$\Delta P = \frac{\sum_{i=0}^{2} a_i \cos^i \gamma}{\mu_S \mu_V R^*} \qquad (1)$$

where R* is the reflectance at 763 nm that would be measured if there were no absorption (see Appendix), γ is the scattering angle, μ_S and μ_V are the cosine of the solar and the satellite zenith angles respectively. The a_i (i = 0, 2) coefficients are determined from simulations of radiative transfer through a clear atmosphere above various surfaces.

The sum $P_{app} + \Delta P$ is reported in figure 4. For the stratocumulus and cirrus cases, ΔP is only about 7-8 hPa. For the clear-ocean case, ΔP is about 13 hPa near the sun-glint direction but as large as 300 hPa far from that direction. Now, using a threshold on $P_{app} + \Delta P$ allows to identify as cloudy the pixels of which the pressure appears lower than 900 hPa. Generally speaking, a pixel is assumed to be cloud-contaminated when the pressure $P_{app} + \Delta P$ is significantly weaker than the surface pressure derived from the nearest ECMWF (European Centre for Medium range Weather Forecasts) analysis. In this way, the use of the apparent pressure allows to detect unambiguously thick and high/middle-level clouds. However, pixels remain unclassified in case of clear-sky, very low level clouds, very thin cirrus clouds and broken clouds.

3.4. *Reflectance tests*

In many daytime cloud detection algorithms, a pixel is declared cloudy if the measured reflectance is above some reference value that represents clear-sky conditions. Over ocean, in the absence of glitter effects, the surface is easily distinguished from clouds by its low reflectance, particularly in the near-infrared portion of the spectrum where the signal is less sensitive to molecular and aerosol scattering effects. Figure 5 shows the histograms of the difference R_{865} - R_{865}^{clear} between the measured reflectance at 865 nm and its clear-sky estimate for the POLDER measurements reported in figure 2. Practically, over ocean, the clear-sky reflectance is estimated from radiative transfer simulations by using the sea-surface reflectance model of Cox and Munk (1956) ; the sea-surface wind velocity used in this model is derived from ECMWF analysis. This comparison only concerns the viewing directions outside of the expected region of the solar specular reflection. Note that the

difference $R_{865} - R_{865}^{clear}$ can be slightly negative because our clear-sky model does not correspond to perfectly clean conditions but to a typical aerosol optical thickness of 0.1 . Pixels that present a negative or hardly positive difference (say, weaker than 0.01) can be classified as clear while pixels that present a noticeable difference (say, larger than 0.05) can be classified as cloudy. For intermediate values of $R_{865} - R_{865}^{clear}$ or inside the expected region of the specular reflection, the pixels remain unclassified.

Over land, the test makes use of the reflectance at 670 nm instead of 865 nm because of the high reflectivity of vegetation in the near-infrared. The use of the 670 nm reflectance increases the contrast between land and cloud. The clear-sky reflectance will be derived from a time series of POLDER observations previously analyzed by the POLDER "Land surfaces" processing line (Leroy *et al.* 1996). On account of the possible presence of lakes and rivers, this test does not work when the radiometer is pointing to the expected region of the solar specular reflection ; however, this region is then restricted to a cone of half-angle of 2° instead of 30°. Neither is this test used when there is any risk of sea-ice or snow according to ECMWF analysis, because snow and ice are highly reflecting.

In most cases, the two threshold tests on apparent pressure and on reflectance are sufficient to classify a pixel as clear or cloudy. That is the case for the three situations of figure 2 with the exception of the clear-sky pixels in the sun-glint region. However, these pixels will be labeled as clear by using a multi-directional test (see section 3.8). Nevertheless, these two tests are insufficient when $P_{app} + \Delta P$ is high and $R_{865} - R_{865}^{clear}$ (or $R_{670} - R_{670}^{clear}$) is rather low (say, between 0.01 and 0.05), which is the case of thin clouds or broken clouds over highly reflecting surfaces. Therefore, the following tests based on polarization are added. The polarized reflectance is known to be less sensitive to multiple scattering effects than the total reflectance (Hansen and Travis 1974). So, the polarized reflectance is expected to be much less contaminated by surface contribution.

3.5. *Test on polarization at 443 nm*

The polarized reflectance at 443 nm is mainly related to the atmospheric molecular optical thickness above the observed surface (cloud, land or ocean), assuming that the radiance originating from this surface is negligibly polarized. This assumption may be wrong for particular directions such as that corresponding to the cloud rainbow ($\gamma \sim 140°$) or to the ocean glitter. Therefore the use of the polarized reflectance PR_{443} is restricted to the region of maximum molecular scattering polarization ($80° < \gamma < 120°$) and outside the sun glint area. According to single scattering approximation, one can estimate the molecular optical thickness :

$$\tau_{443} = (16/3)\, \mu_s\, \mu_v\, PR_{443} / (1 - \cos^2 \gamma). \qquad (2)$$

Figure 6 presents the difference $\tau_{443}^{clear} - \tau_{443}$, where τ_{443}^{clear} is the total molecular optical thickness of the atmosphere between the aircraft and the sea-surface for the three situations shown on figure 2 . The histograms present a large dispersion of which a part can be explained by the measurement of polarization from three successive polarized images and the associated difficulty of coregistration. This

defect ought to be reduced with the satellite version of POLDER of which filters are equipped by prisms for better superposition of the images. Another effect that can bias the measurements comes from the polarization of the observed surface (cloud, land or ocean) which can be slightly different from 0. Nevertheless, in figure 6, the cirrus cloud histogram noticeably differs from the clear-sky one and it clearly appears that a threshold on the $\tau_{443}^{clear} - \tau_{443}$ difference allows to discriminate cirrus-free pixels from others. With the spaceborne version of the instrument, this test is expected to help to detect not only high-level clouds but also middle-level clouds.

3.6. *Test on polarization at 865 nm*

The typical feature of polarization by liquid water clouds in the rainbow direction (near 140°) clearly appears in figure 2 for the stratocumulus clouds. Such high values of polarized signal in the 865 nm channel, that is hardly affected by the molecular scattering are not observed for clear-sky conditions, except in the sun-glint region. Therefore, when the scattering angle is within the range 135^o - 150^o and outside the sun-glint region, low/middle-level clouds can be detected when the polarized reflectance at 865 nm is large enough (figure 7). As written in section 3.4 the polarized reflectance is less sensitive to multiple scattering effects than the total reflectance, i.e. the polarized light is mainly formed by the single scattering process. According to this approximation and for large enough cloud optical thickness one can show that the corrected polarized reflectance term, $(\mu_s + \mu_v)\ PR_{865}$, is less sensitive to μ_v and μ_s than PR_{865} and is mainly governed by the scattering angle. Consequently, a pixel will be labeled as cloudy when the $(\mu_s + \mu_v)\ PR_{865}$ value is large enough.

Note that the threshold value on corrected polarized reflectance has to be higher over land than over ocean. Clear-sky observations over the "La Crau" site in southern France have been reported by Deuze *et al.* (1993) : for scattering angles within 135^o - 150^o, the $(\mu_s + \mu_v)\ PR_{865}$ values were in the range 0.002 - 0.02 , that is significantly higher than over clear ocean.

3.7. *Near-infrared / Visible test*

The four previous tests should allow the detection of a lot of cloud-filled POLDER pixels. On the other hand, when all the tests of cloud detection prove negative, two additional tests are operated in order to identify pixels that are definitely clear. The first of these tests has already been presented in section 3.4. It is a reflectance threshold test applied to the 865 nm or to the 670 nm bidirectional reflectance over sea or land respectively. Pixels that present a negative or hardly positive difference between the measured reflectance and its clear-sky estimate are classified as clear.

The last of the tests that are applied pixel by pixel and direction by direction uses the spectral variability of the reflectance. As the reflectance hardly varies from 670 nm to 865 nm over clouds and the anisotropy effects are similar in both channels, the ratio of near-infrared reflectance to visible reflectance is always close to unity over clouds. On the contrary, the ocean color or the presence of vegetation over land can induce difference between 670 and 865 nm reflectances. Then, a pixel can be labeled as clear when the reflectance at 865 nm is significantly different from the one at 670 nm, i.e. when the ratio is different from 1. This additional test is similar to the one

used in operational AVHRR algorithms (e.g., Saunders and Kriebel 1988, Stowe *et al.* 1991).

3.8. *Multi-directional and spatial tests*

When applying the different threshold tests to the POLDER pixels, in some cases, the pixel remains unclassified for a given direction. For instance when some of the viewing directions correspond to the sun-glint area, the pixel is labeled undetermined for those directions whereas it has been declared as cloud-filled or cloud-free in the other ones (figure 8). Therefore, if the pixel is labeled as cloudy (or clear) in some directions and undetermined in all the other ones, then it is labeled as cloudy (or clear) for all the directions. Clearly, that multi-directional test chiefly concerns the cases with possible sun-glint but can be useful for broken cloud or thin cirrus situation.

At this stage, a pixel can remain undetermined in a given direction if the pixel appears cloudy from one direction and clear from another or if the pixel is undetermined whatever the direction. For that direction, the pixel is classified as clear or cloudy by utilizing the spatial information at the scale of a "super-pixel" (see section 2) composed of 81 pixels. If the super-pixel contains some clear and cloudy pixels in the direction, the undetermined ones are relabeled as clear or cloudy according to whether $(R_{670} - < R_{670}^{clear} >) / \sigma_{670}^{clear}$ is lower or higher than $(R_{670} - < R_{670}^{cloudy} >) / \sigma_{670}^{cloudy}$, where $< R_{670}^{clear} >$ and $< R_{670}^{cloudy} >$ are the mean reflectances of the clear and cloudy pixels respectively, and σ_{670}^{clear} and σ_{670}^{cloudy} are their associated standard deviations. In the few cases where all the pixels are undetermined, they are all relabeled as clear or cloudy depending on the spatial variability of the reflectance at 865 nm (over ocean) or 670 nm (over land). Indeed, aerosols are expected to present a lower spatial variability of the reflectance than clouds. However, that test cannot be used when there is sea-ice or snow risk ; in that case, the cloudiness diagnosed by ECMWF will be used to allow the continuation of the data processing. Of course, these doubtful cases will be flagged.

Classification in cloud-filled and cloud-free pixels is then followed by the derivation of the cloud cover of each super-pixel. First, the cloud amount is determined direction by direction and then the averaged cloudiness is computed. The percentage of pixels undetermined at the end of the first series of tests as well as the variation of the cloud cover from direction to direction will indicate the reliability of the averaged cloud cover.

Cloud parameters (i.e. optical thickness, pressure, phase) can then be inferred from the cloud-filled radiances as explained in the following sections. For pixels labeled as clear for all viewing directions, the water vapor content is determined as in the POLDER "Land surfaces" processing line (Leroy *et al.* 1996). Over ocean, this determination will be restricted to the case of high surface reflectivity, that is for sunglint conditions.

4. Retrieval of cloud properties

4.1. *Cloud optical thickness*

Cloud optical thickness is directly related to the total condensed water content and is thus a crucial parameter in cloud modeling. Despite of POLDER multi-directional capabilities, the derivation of cloud optical thickness remains very close to that of the first ISCCP cloud analysis (Rossow and Schiffer 1991) and assumes a homogeneous plane-parallel cloud layer composed of water drops with an effective radius of 10 μm and an effective variance of 0.15 (Hansen and Travis 1974) ; the difference is that this retrieval is done for up to 14 viewing directions. This choice is supported by two reasons : (i) the objective of these algorithms which are called of class 1 is to provide a series of products that are robust and that can be validated rapidly, (ii) the comparison of the optical thicknesses retrieved for ~14 viewing directions will allow a test of the validity of the model. It is our opinion that a considerable step forward would be made if, for example, one would be able to evaluate at global scale to which extent and under which conditions the plane parallel hypothesis fails at representing radiative properties of liquid water clouds. It should be possible to make some progress in this direction by simply testing the consistency of the retrieved optical thickness according to the direction of observation. Cloud optical thickness is thus determined for each viewing direction and each pixel. However, as mentioned in section 2, cloud optical thicknesses as well as all the other products are finally averaged at the "super-pixel" scale, i.e. on a 9 x 9 pixel area.

The relation between the reflectance at top of the atmosphere R_λ (λ = 443, 670 and 865 nm) and the cloud optical thickness is dependent on the surface reflectivity. For land scenes, the surface reflectance is obtained from surface parameters previously retrieved from POLDER observations under clear-sky conditions by the POLDER "Land surfaces" processing line (Leroy *et al.* 1996). For ocean scenes, the surface reflectance is calculated using the Cox and Munk (1956) model depending on the surface wind velocity derived from ECMWF analysis. The surface anisotropy can have an important effect on the light "directly" reflected by the surface without any scattering in the atmosphere ; but it is assumed to have a neglectible effect on the "diffuse" light scattered by the atmosphere. Consequently, the reflectance R_λ is decomposed into a direct part calculated using the bidirectional surface reflectance $\rho_\lambda^{surface}(\mu_s, \mu_v, \phi)$ and a diffuse part calculated using the hemispherical surface reflectance (or albedo) $\alpha_\lambda^{surface}(\mu_s)$:

$$\begin{aligned} R_\lambda &= R_\lambda^{direct} + R_\lambda^{diffuse} \\ &= \rho_\lambda^{surface}(\mu_s, \mu_v, \phi)\ e^{-\left(\frac{1}{\mu_s} + \frac{1}{\mu_v}\right)\delta_\lambda} + R_\lambda^{diffuse}(\mu_s, \mu_v, \phi, \alpha_\lambda^{surface}, \delta_\lambda) \end{aligned} \qquad (3)$$

where δ_λ is the scaled total optical thickness taking into account the sharp diffraction peak near 0° scattering angle (Potter 1970). Practically, off-line calculations of reflectance are performed for various conditions of viewing/illumination geometry, surface albedo and cloud optical thickness by using the discrete ordinate method (Stamnes *et al.* 1988). The value of $R_\lambda^{diffuse}$ is then interpolated for the observation conditions. Then, R_λ values are obtained from (3) for various values of δ_λ. It results

in a table of reflectances from which the optical thickness is interpolated.

Finally only the optical thickness at 670 nm is preserved in the products ; the values at 443 and 865 nm are used as indicators of the reliability of the 670 nm optical thickness. Individual optical thicknesses are averaged on the cloudy pixels of a super-pixel. Variation of the cloud optical thickness from pixel to pixel will be a key information on the horizontal cloud heterogeneity. On the other hand, comparisons of the optical thickness from direction to direction will provide information on the validity of our model.

Using the POLDER images acquired just before and after those presented on figure 2, 14 values of cloud optical thickness were determined for each target of 9 x 9 pixels from the 865 nm reflectance values measured in 14 different viewing directions. The mean and the standard deviation of the 14 optical thicknesses of each cloudy target were computed ; the histograms are reported on figure 9. Figure 9a shows that the spatial variability of the optical thicknesses is notably higher for the stratocumulus than for the cirrus, as expected from the reflectance pictures (see figure 2b). The non-zero standard deviation of the optical thickness (figure 9b) is chiefly related to the weakness of the plane-parallel approximation for the stratocumulus and to the wrong hypothesis of spherical water drops in the case of the cirrus. Due to the non-linear relationship between optical thickness and reflected flux, the effect of the angular dispersion of the optical thickness is rather difficult to interpret. The hemispherical reflectance (or albedo) which is independent of the direction of observation is easily calculated from the optical thickness (see further section 4.4). It is interesting to check the angular dependence of the albedo retrieved from POLDER measurements. Histograms of the standard deviation of the 865 nm albedo are reported on figure 10. The two clouds under study are compared to a stratocumulus deck selected for its homogeneous aspect in Descloitres *et al.* (1995). For this almost ideal case, the angular dispersion of the retrieved albedo is close to 0.01, a large part of which is certainly due to the instrument and algorithm noises. This dispersion varies from 0.01 up to more than 0.05 for the heterogeneous stratocumulus cloud and is close to 0.035 for the cirrus cloud. An albedo error of 0.035 typically corresponds to a SW flux error of 30 Wm^{-2}, that is quite significant for ERB studies. That clearly emphasizes importance of departure from the model for the more heterogeneous parts of the stratocumulus layer and for the ice cloud. Note that these results have been performed from 20 m-size pixels ; they might be different for satellite observations at the 6 km-resolution since the effects of cloud inhomogeneities can depend strongly on the scale of the observations.

4.2. *Cloud pressure*

Together with cloud optical thickness which regulates the influence of clouds on the terrestrial albedo, one of the most important cloud properties with respect to global climate changes is cloud height - or cloud pressure. For instance, Ohring and Adler (1978) found that an increase of 1 km in cloud height would result in a 1.2 K increase in surface temperature. Several techniques for deriving cloud altitude from satellite have already been developed, among them the well-known brightness temperature technique (Stowe *et al.* 1988), the CO_2 slicing technique introduced by Smith and Platt (1979) or the analysis of backscattered radiances within the Oxygen A band

introduced by Yamamoto and Wark (1961). In the present scheme, two methods are used. The first one makes use of the ratio of the two POLDER radiances measured in the Oxygen A band. The second one is based on the analysis of polarized reflected sunlight at 443 nm.

4.2.1. *Cloud pressure derived from O_2 absorption*

As already stated in section 3.3, the apparent pressure differs from the cloud top pressure because of the effect of surface reflection and multiple scattering inside the cloud. For a cloud layer thick enough for the surface influence to be negligible, the apparent pressure P_{app} becomes mainly dependent on the vertical distribution of liquid water and is practically always situated between the cloud top level and the cloud base one, so that we can call it the "cloud pressure". In case of a thin cloud layer, a significant if not preponderant amount of photons can reach the ground surface and be reflected back to space. In this case, the apparent pressure can be outside of the cloud layer limits. Here, we remove the surface effect from the apparent pressure and the "cloud pressure" P_{cloud} is thus defined as the apparent pressure that would be observed if the surface reflectivity were equal to zero.

In first approximation, the transmission of the oxygen A band can be treated by means of a random band model composed of strong lines (Goody 1964) so that :

$$T_{O2} = \exp\left(-\,C\sqrt{m}\;P_{app}\right), \qquad (4)$$

where m is the air-mass factor and C is a constant depending on spectroscopic data. Schematically, T_{O2} can be decomposed into a term corresponding to the light directly reflected by the cloud and a term corresponding to the light reflected after reaching the surface (figure 11). Let $r = R^{**} / R^{*}$, where R^{*} is the reflectance measured near 763 nm without gaseous absorption and R^{**} is the reflectance that would be measured if in addition the surface was black. Then,

$$\exp\left(-\,C\cdot\sqrt{m}\;P_{app}\right) = r\,\exp\left(-\,C\cdot\sqrt{m}\;P_{cloud}\right) + (1-r)\exp\left(-\,C\sqrt{\left\{m\,P_{cloud}^2 + M\left(P_{surface}^2 - P_{cloud}^2\right)\right\}}\right) \qquad (5)$$

where $P_{surface}$ is the surface pressure and M is an "effective" air-mass factor corresponding to the mean photon path between the cloud and the surface. Practically, M is approximated by a bilinear function of m and r from numerical simulations of the photon path calculated for various surface reflectances and various cloud optical thicknesses (figure 12).

In practice, R^{*} results from the correction algorithm (see Appendix), R^{**} is computed by using the previously derived cloud optical thickness and $P_{surface}$ is obtained from ECMWF analysis. Thus, P_{cloud} is derived from P_{app} by inverting (5). Note that the random band model is only used to derive the "cloud pressure" from the apparent pressure. The derivation of the apparent pressure is based on a line-by-line model (see section 3.3).

However, in case of thin cloud layer over surface with high reflectivity near 763 nm, P_{cloud} may remain undetermined because of the impossibility to solve (5) due to radiometric and algorithmic noises. Moreover, as P_{cloud} is more reliable when a variation of P_{app} induces a smaller variation of P_{cloud}, the values of P_{cloud} are weighted by the derivative $\partial P_{app}/\partial P_{cloud}$ when averaged at the super-pixel scale.

4.2.2. *Cloud pressure derived from polarization at 443 nm*

In this approach, the cloud pressure is retrieved from the polarization measurements at 443 nm. As already outlined in section 3.5, for scattering angles γ ranging from 80° to 120° and outside the sunglint direction, it chiefly corresponds to the light scattered by the molecular layer above the cloud. There is, however, a small contamination by the cloud layer itself. This effect is removed from the polarization measurement at 443 nm by using that at 865 nm where molecular scattering is negligible. Thus, we first calculate the optical thickness $\tau_R^{(0)}$ by using this corrected polarized reflectance instead of PR_{443} in equation (2). Then we derive a better estimate of the molecular optical thickness τ_R by taking into account multiple scattering within molecular layers. Based on off-line calculations, τ_R is obtained by using a polynomial function of $\tau_R^{(0)}$, m , $\cos\gamma$ and $\sin\phi$, where ϕ is the relative azimuth angle. The "Rayleigh" cloud pressure is then directly proportional to τ_R .

Figure 13 compares the Rayleigh cloud pressure to that derived from O_2 absorption for the two cloudy cases of figure 2. The root mean square difference is 50 hPa and 100 hPa for the cirrus and the stratocumulus cloud respectively. Considering the calibration and coregistration uncertainties of the airborne simulator, the agreement is satisfactory. However, in case of cloud layers much thinner than those presented on figure 12, it is to be feared that the retrieved Rayleigh pressure - and even more the retrieved O_2 pressure - differ significantly from the actual cloud pressure. Therefore, the pressure value will be preserved only when the cloud optical thickness will be large enough (say 1 or 2).

4.3. *Cloud thermodynamic phase*

Cloud phase recognition is important for cloud studies. Ice crystals correspond to physical process and present optical properties that differ from those of liquid water drops. The angular polarization signature of clouds will, in some cases, help at discriminating between liquid and solid phases of cloud particles. Liquid cloud droplets exhibit the very specific polarization feature of the rainbow for scattering angles near 140°. Conversely, theoretical studies of scattering by various crystalline particles (prisms, hexagonal crystals) all show that the rainbow characteristic disappears as soon as the particles depart from spherical geometry (Cai and Liou 1982, de Haan 1987, Brogniez 1992). Thus, the presence or absence of this characteristic feature in cloud polarized reflectance should indicate the presence or absence of liquid water and conversely that of crystals. This is clearly supported by figure 2. Nonetheless, the angular dependence of cloud polarized reflectances may be influenced by other factors such as cloud heterogeneity. In these conditions, it is likely that cloud phase will not always be determined unambiguously : since the rainbow is

typical of liquid drops, then its presence allows to conclude to the presence of liquid water, but the reverse is not true. Consequently, the phase cannot be determined for all the cloudy pixels.

For scattering angles in the range 135° - 150° outside the sunglint region, $(\mu_s + \mu_v)$ PR_{865} is compared to two values F_{max} and F_{min} (figure 14). When $(\mu_s + \mu_v)$ PR_{865} is larger than F_{max} , the phase is assumed to be liquid. When $(\mu_s + \mu_v)$ PR_{865} is weaker than F_{min} , the phase is expected to be ice. In the other cases, both ice and liquid water clouds may occurs and the phase will remain undetermined. As a precaution, the phase will not be determined either in case of very tenuous cloud layer with optical thickness lower than ~ 1.

4.4. *Cloud albedo*

Unlike the bidirectional reflectance, the directional reflectance (or albedo) is independent of the direction of observation. As already noted in 4.1, it is interesting to check the angular dependence of the albedo retrieved from POLDER measurements under the assumption of a plane-parallel cloud layer composed of spherical droplets. So, cloud albedo is determined for each viewing direction.

Moreover, estimate of the cloud forcing is of prime importance for climate study. The SW cloud forcing is directly related to the difference between the observed SW albedo and its clear-sky estimate. Thus, we attempt to determine the narrow-band albedo in several channels of POLDER and then to estimate the albedo integrated over the whole range of the solar spectrum.

The albedo at 443, 670 and 865 nm - without gaseous absorption - is calculated off-line as a function of solar elevation, surface reflectance and cloud optical thickness. For each channel noted j, it results in a table from which the albedo A_j is interpolated by using the previously derived cloud optical thickness.

Then the SW albedo is estimated from these narrow-band albedoes as

$$A_{SW} = f_{443}\, A_{443} + f_{670}\, A_{670} + f_{865}\, A_{865} \qquad (6)$$

where f_{443} and f_{670} are functions of the total ozone amount measured from TOMS (Total Ozone Mapping Spectrometer) onboard ADEOS and f_{865} depends on the water-vapor content and is approximated by a linear function of the R_{910}/R_{865} ratio. These weighting functions f_j are fitted from simulations using a radiative transfer code with 4750 spectral intervals between 0.2 and 4 μm ; the radiative transfer equation was solved using the discrete ordinate method and the interactions between scattering and molecular absorption were accounted for by exponential sums fitting the molecular absorption. Various atmospheres and ground surfaces were considered. The major uncertainty concerns the cloud optical properties ; for consistency with the optical thickness derivation, clouds were assumed to be composed of spherical droplets with an effective radius of 10 μm.

In order to evaluate the SW cloud forcing, the clear-sky values A_j^{clear} of the cloudy areas need to be estimated. This is done by assuming a cloud optical thickness equal to zero. The corresponding SW clear-sky albedo A_{SW}^{clear} is calculated as in (6) by

replacing f_{865} by a function of the water vapor content derived from ECMWF analysis.

In a similar way, the SW bidirectional reflectances are estimated from the measured narrow-band bidirectional reflectances. That should be useful for ERB studies. However, these integrations over the whole spectrum will remain speculative as long as they are not validated from ERB scanner measurements.

5. Conclusion

POLDER presents some specific capabilities that make it a powerful tool to investigate cloud properties and to improve the accuracy of Earth Radiation Budget measurements : namely, its multispectral, angular and polarization capabilities. The "ERB & clouds" algorithms have been designed so as to take advantage of these new possibilities. The objective when designing the present algorithms has been to reduce the validation time ; the consequence is that a full exploitation of POLDER capabilities has not been completely possible. This will be the case of a second class of algorithms which will be developed after the validation of this first class. However, it should already be possible to make significant progress, for example by testing the consistency of the retrieved optical thickness according to the viewing direction. Thus, one would be able to evaluate at global scale to which extent and under which conditions the plane parallel hypothesis fails at representing radiative properties of liquid water clouds.

The present algorithms for the cloud detection and the derivation of cloud properties have been developed from the experience acquired by analyzing POLDER airborne measurements made during several campaigns such as EUCREX'94. However, the various thresholds introduced in these algorithms have to be adjusted and afterwards controlled.

A series of validation plans have been designed. They are based on (1) the checking of consistency between the different output data, such as the cloud covers determined from different viewings of a given super-pixel, the two cloud pressures derived from O_2 absorption and from polarization respectively, etc. and (2) the comparison with quantities derived from fully independent data.

The cloud detection algorithm has to be severely monitored since it plays a crucial role in the cloud properties determination. The dynamic cluster analysis method developed by Desbois *et al.* (1982) and improved by Raffaelli and Seze (1995) has been selected mainly because it is a robust and very different method which does not make use of thresholds. Full resolution visible and thermal infrared data from geostationary satellites at the ADEOS crossing time will be used and, as soon as available, those from OCTS (Ocean Color and Temperature Scanner) on ADEOS. The cloud classification results will be averaged at the POLDER super-pixel resolution and the cloud cover derived from POLDER can thus be tested. In the same way, the Rayleigh and the O_2 cloud pressure can be compared to that derived from the radiative temperature by using ECMWF atmospheric profiles.

The cloud pressure and optical thickness derived from POLDER will be also compared to the ISCCP data. The BRDFs will be compared with the ERBE ones and the short-wave albedo with coincident Meteor / ScaRaB measurements (Kandel *et al.* 1994), if possible.

These validations will be conducted under the control of the International POLDER

Scientific Team.

Acknowledgments

This work was supported by the French Centre National d'Etudes Spatiales. The authors wish to thank F. Lemire for data processing, J. Descloitres for derivation of cloud optical thickness, P. Flamant and J. Pelon for lidar data, F. M. Breon, P. Dubuisson and J. P. Duvel for helpful discussions and A. Lifermann for her comments on the manuscript.

Currently updated information about POLDER project is available from http://earth-sciences.cnes.fr:8060/

Appendix : Correction for gaseous absorption and stratospheric aerosol effect

Measured radiances are first corrected for primary scattering by stratospheric aerosol. Stratospheric aerosol optical thickness will be regularly updated from SAGE (Stratospheric Aerosol and Gas Experiment) measurements. This correction, which remains insufficient in case of a major volcanic event, affects scarcely the unpolarized radiance values but are necessary for the polarized ones which correspond chiefly to the first order of scattering.

Typical values of gaseous absorption in the different channels used in the "ERB & clouds" processing line are reported in table A-1. Radiances in channels centered at 443, 670, 765 and 865 nm are weakly affected by absorption while radiances at 763 and 910 nm are selected for their strong absorption by oxygen and water vapor lines respectively.

Ozone absorption is removed by calculating the transmissions as functions of mU_{O3}, where m is the air-mass factor and U_{O3} is the column abundance of ozone measured from TOMS. The water vapor absorption of the 865 nm channel is corrected according to a function of the ratio of the 910 and 865 nm reflectances R_{910}/R_{865}. The parameterizations of ozone and water vapor transmissions are derived from simulations using a line-by-line model (Scott 1974).

A particular treatment concerns the 763 nm and 765 nm channels. The reflectance R* that would be measured if there was no absorption is assumed to be the same in both channels. The R_{763} and R_{765} measured reflectances can be written respectively as :

$$R_{763} = R^*. T_{O2} . T'_{H2O} . T'_{O3} \quad (A1)$$

$$R_{765} = A\, R_{763} + (1-A). R^* . T''_{H2O} . T''_{O3} \quad (A2)$$

where the constant A may be considered as the percentage of the wide spectral band where oxygen lines are located (figure A1) ; its value derived from line-by-line simulations is close to 0.3. The ozone transmittances T'_{O3} and T''_{O3} are parameterized as functions of $m\ U_{O3}$. The water vapor transmittances T'_{H2O} and T''_{H2O} are approximated by a function of the R_{910}/R_{865} ratio. Finally, the oxygen transmittance T_{O2} and the reflectance R* which is assumed to be the same in both channels, can be derived by combining (A1) and (A2)

References

BALDWIN, D. G. and COAKLEY Jr., J. A., 1991, Consistency of Earth radiation budget experiment bidirectional models and the observed anisotropy of reflected sunlight, *Journal of Geophysical Research*, **96**, 5195-5207.

BARKSTROM, B. R., HARRISON, E. F. and LEE, R. B., 1990, Earth Radiation Budget Experiment. Preliminary seasonal results, *EOS*, **71**, 297-305.

BROGNIEZ, G., PAROL, F., BURIEZ, J. C. and FOUQUART, Y., 1992, Bidirectional reflectances of cirrus clouds modelized from observations during the International Cirrus Experiment 89, in *Proceedings of International Radiation Symposium*, Tallin, 133-136.

BROGNIEZ, G., 1992, Contribution ‡ líÈtude des propriÈtÈs optiques†et radiatives des cirrus, ThËse d'Etat, UniversitÈ des Sciences et Technologies de Lille, France.

CAI, Q. and LIOU, K. N., 1982, Polarized light scattering by hexagonal ice cristals: theory, *Appllied Optics*, **21**, 3569-3580.

CESS, R. D., POTTER, G. L., BLANCHET, J. P., BOER, G. J., DEL GENIO, A. D., DEQUE, M., DYMNIKOV, V., GALIN, V., GATES, W. L., GHAN, S. J., KIEHL, J. T., LACIS, A. A., LE TREUT, H., LI, Z. X., LIANG, X. Z., MCAVANEY, B. J., MELESHKO, V. P., MITCHEL, J. F. B., MORCRETTE, J.-J., RANDALL, D. A., RIKUS, L., ROECKNER, E., ROYER, J. F., SCHLESE, U., SHEININ, D. A., SLINGO, A., SOKOLOV, A. P., TAYLOR, K. E., WASHINGTON, W. M., WETHERALD, R. T., YAGAI, I. and ZHANG, M. H., 1990, Intercomparison and interpretation of climate feedback processes in 19 atmospheric general circulation models, *Journal of Geophysical Research*, **95**, 16601-16616.

CHAPMAN, R. M., 1962, Cloud distributions and altitude profiles from satellite, *Planetary Space Science*, **9**, 70-71.

COESA, 1976, *U. S. Standard Atmosphere, 1976*, U. S. Government Printing Office, Washington, D. C.

COX, C. and MUNK, W., 1956, Slopes of the sea surface deduced from photographs of the sun glitter, *Bulletin of the Scripps Institute of Oceanography*, **6**, 401-488.

DE HAAN, J., 1987, Effects of aerosols on the brightness and polarization of cloudless planetary atmospheres, M. S. Thesis, Free University of Amsterdam, Netherlands.

DESBOIS, M., SEZE, G. and SZEJWACH, G., 1982, Automatic classification of clouds on Meteosat imagery : Application to high-level clouds, *Journal of Applied Meteorology*, **21**, 401-412.

DESCHAMPS, P. Y., BREON, F. M., LEROY, M., PODAIRE, A., BRICAUD, A., BURIEZ, J.-C. and SEZE, G., 1994, The POLDER mission: Instrument characteristics and scientific objectives, *IEEE Transactions on Geoscience and Remote Sensing*, **32**, 598-615,.

DESCLOITRES, J., PAROL, F. and BURIEZ, J.-C., 1994, On the validity of the plane-parallel approximation for cloud reflectances as measured from POLDER during ASTEX," *Annales Geophysicae*, **13**, 108-110,.

DESCLOITRES, J., BURIEZ, J.-C., PAROL, F. and VANBAUCE, C., 1995, About cloud reflectances as measured from POLDER during CLEOPATRA, ASTEX and EUCREX, *Atmospheric Sensing and Modeling II*, Richard P. Santer, Editor, Proc. SPIE 2582, 253-263.

DEUZE, J.-L., BREON, F. M., DESCHAMPS, P.-Y., DEVAUX, C. and HERMAN, M., 1993, Analysis of the POLDER (POLarization and Directionality of Earth's Reflectances) airborne instrument observations over land surfaces, *Remote Sensing of Environment*, **45**, 137-154.

FISHER, J. and GRASSL, H., 1991, Detection of cloud-top height from backscattered radiances within the Oxygen A band. Part 1: Theoretical study, *Journal of Applied Meteorology*, **30**, 1245-1259.

FISHER, J., CORDES, W., SCHMITZ-PEIFFER, A., RENGER, W. and MˆRL, P., 1991, Detection of cloud-top height from backscattered radiances within the Oxygen A band. Part 2: Measurements, *Journal of Applied Meteorology*, **30**, 1260-1267.

GOLOUB, P., DEUZE, J. L., HERMAN, M. and FOUQUART, Y., 1994, Analysis of the POLDER polarization measurements performed over cloud covers, *IEEE Transactions on Geoscience and Remote Sensing*, **32**, 78-88.

GOODY, R. M., 1964, *Atmospheric Radiation I. Theoretical Basis*, Clarendon Press, Oxford.

HAN, Q., ROSSOW, W. B. and LACIS, A. A., 1994, Near-global survey of effective droplet radii in liquid water clouds using ISCCP data, 1994, *Journal of Climate*, **7**, 465-497.

HANSEN, J. E. and TRAVIS, L. D., 1974, Light scattering in planetary atmospheres, *Space Science Review*, **16**, 527-610.

KANDEL, R. S., MONGE, J. L., VIOLLIER, M., PAKHOMOV, L. A., ADASKO, V. I., REITENBACH, R. G., RASCKHE, E. and STUHLMANN, R., 1994, The ScaRaB project : Earth radiation budget observations from the Meteor satellites, *Advances in Space Research*, **14**, 147-154.

LEROY, M., DEUZE, J.-L., BREON, F.-M., HAUTECOEUR, O., HERMAN, M., BURIEZ, J.-C., TANRE, D., BOUFFIES, S., CHAZETTE, P. and ROUJEAN, J.-L., 1996, Retrieval of atmospheric properties and surface bidirectional reflectances over the land from POLDER/ADEOS, *Journal of Geophysical Research*, to appear.

O'BRIEN, D. M. and MITCHELL, R. M., 1992, Error estimates for retrieval of cloud-top pressure using absorption in the A band of Oxygen, *Journal of Applied Meteorology*, **31**, 1179-1192.

OHRING, G. and ADLER, S., 1978, Some experiments with a zonally averaged climate model, *Journal of Atmospheric Sciences*, **35**, 186-205.

PAROL, F., BURIEZ, J.-C., CRÈTEL, D. and FOUQUART, Y., 1994 a, The impact of cloud inhomogeneities on the Earth radiation budget: The 14 October 1989 I.C.E. convective cloud case study, *Annales Geophysicae*, **12**, 240-253.

PAROL, F., GOLOUB, P., HERMAN, M. and BURIEZ, J.-C., 1994 b, Cloud altimetry and water phase retieval from POLDER instrument during EUCREX'94, in *Atmospheric Sensing and Modelling*, Richard P. Santer, Editor, Proc. SPIE 2311, 171-181.

POTTER, J. F., 1970, The Delta function approximation in radiative transfer theory, *Journal of Atmospheric Sciences*, **27**, 943-949.

RAFFAELLI, J. L. and SEZE, G., 1995, Clouds type separation using local correlation between visible and infrared satellite images, in *Proceedings of the 7th EUCREX Workshop*, Villeneuve d 'Ascq, France, G. Brogniez Ed., 123-133.

ROSSOW, W. B., GARDER, L. C. and LACIS, A. A., 1989, Global, seasonal clouds variations from satellite radiance measurements. Part I: sensitivity of analysis, *Journal of Climate*, **2**, 419-458.

ROSSOW, W. B. and SCHIFFER, R. A., 1991, ISCCP cloud data products, *Bulletin of the American Meteorological Society*, **6**, 2394- 2418.

SAUNDERS, R. W. and KRIEBEL, K. T., 1988, An improved method for detecting clear sky and cloudy radiances from AVHRR data, *International Journal of Remote Sensing*, **9**, 123-150.

SCOTT, N. A., 1974, A direct method of computation of the transmission function of an inhomogeneous gaseous medium. I: description of the method, *Journal of Quantitative Spectroscopy and Radiative Transfer*, **14**, 691-704.

SENIOR, C. A. and MITCHELL, J. F. B., 1993, Carbon dioxide and climate : The impact of cloud parameterization, *Journal of Climate*, **6**, 393-418.

SMITH, W. L. and PLATT, C. M. R., 1979, Comparison of satellite-deduced clouds heights with indications from radiosonde and ground-based laser measurements, *Journal of Applied Meteorology*, **17**, 1796-1802.

STAMNES, K., TSAY, S. C., WISCOMBE W. J. and JAYAWEERA, K., 1988, Numerically stable algorithm for discrete-ordinate-method radiative transfer in multiple scattering and emitting layered media, *Applied Optics*, **27**, 2502-2509.

STOWE, L. L., WELLWMEYER, C. G., ECK, T. F., YEH, H. Y. M. and the NIMBUS-7 CLOUD DATA PROCESSING TEAM, 1988, Nimbus-7 global cloud climatology. Part I: algorithms and validation, *Journal of Climate*, **1**, 445-470.

STOWE, L. L., MCCLAIN, E. P., CAREY, R., PELLEGRINO, P., GUTMAN, G. G., DAVIS, P., LONG, C. and HART, S., 1991, Global distribution of cloud cover derived from NOAA/AVHRR operational satellite data, *Advances in Space Research*, **11**, 351-354.

SUTTLES, J. T., GREEN, R. N., MINNIS, P., SMITH, G. L., STAYLOR, W. F., WIELICKI, B. A., WALKER, I. J., YOUNG, D. F., TAYLOR, V. R. and STOWE, L. L., 1988, Angular radiation models for Earth-atmosphere system, volume I- Shortwave radiation, NASA RP-1184.

WEILL, A., BAUDIN, F., DUPUIS, H., EYMARD, L., FRANGI, J.-P., GERARD, E., DURAND, P., BENECH, B., DESSENS, J., DRUIHET, A., RECHOU, A., FLAMANT, P., ELOURAGINI, S., VALENTIN, R., SEZE, G., PELON, J., FLAMANT, C., BRENGUIER, J.-L., PLANTON, S., ROLLAND, J., BRISSON, A., LE BORGNE, P., MARSOUIN, A., MOREAU, T., KATSAROS, K., MONIS, R., QUEFFEULOU, P., TOURNADRE, J., TAYLOR, P. K., KENT, E., PASCAL, R., SCHIBLER, P., PAROL, F., DESCLOITRES, J., BALOIS, J.-Y., ANDRE, M. and CHARPENTIER, M., 1995, SOFIA 1992 experiment during ASTEX, *The Global Atmosphere and Ocean System*, **3**, 355-395.

WIELICKI, B. A., CESS, R. D., KING, M. D., RANDALL, D. A. and HARRISON, E. F., 1995, Mission to Planet Earth : role of clouds and radiation in climate, *Bulletin of the American Meteorological*

Society, **76**, 2125-2153.
YAMAMOTO, G. and WARK, D. Q., 1961, Discussion of the letter by R. A. Hanel: Determination of cloud altitude from a satellite, *Journal of Geophysical Research*, **66**, 3596.

Table 1. Characteristics of the spectral bands of the POLDER instrument. There are 3 channels for each polarized band. The channels with low dynamic range of reflectance are not used in the "ERB & clouds" processing line. Only the bands indicated by an asterix were present in the airborne POLDER instrument during the EUCREX'94 campaign.

Central Wavelength	Band width	Polarization	Dynamic range
443 nm	20 nm	no	0 - 0.22
443 nm (*)	20 nm	yes	0 - 1.1
490 nm	20 nm	no	0 - 0.17
565 nm	20 nm	no	0 - 0.11
670 nm	20 nm	yes	0 - 1.1
763 nm (*)	10 nm	no	0 - 1.1
765 nm (*)	40 nm	no	0 - 1.1
865 nm (*)	40 nm	yes	0 - 1.1
910 nm (*)	20 nm	no	0 - 1.1

Table 2. POLDER level 2 "ERB & clouds" product provided for each orbit at the super-pixel scale:

PARAMETER	***Description***
General information	*ïNumber of elementary pixels* N_{pixels} *ïNumber of viewing directions* N_{dir} *ïViewing/illumination geometry* *ïQuality indices, etc.*
REFLECTANCES at 443, 670, 865 nm and SW estimate	*ï* N_{dir} *spatially averaged values*
ALBEDOES at 443, 670, 865 nm and SW estimate	*ïMean and standard deviation of* N_{dir} *x* N_{pixels} *values* *ïStandard deviation of the* N_{dir} *spatially averaged values* *ïStandard deviation of the* N_{pixels} *angularly averaged values* *ïMean of the clear-sky estimates*
CLOUD COVER	*ïFraction derived from the* N_{dir} *x* N_{pixels} *values and accuracy* *ï* N_{dir} *fractions derived from the* N_{pixels} *values*
WATER VAPOR CONTENT (only for clear-sky conditions)	*ïMean and quality index*
CLOUD OPTICAL THICKNESS (simple linear average and energy-weighted average) O_2-APPARENT PRESSURE O_2-CLOUD PRESSURE RAYLEIGH-CLOUD PRESSURE	*ïMean and standard deviation* *ï* N_{dir} *spatially averaged values (means and standard deviations)* *ïDistribution in 42 optical thickness / pressure classes*
CLOUD PHASE	*ïIndex (Liquid, Ice, Mix, Undeterminated, Not calculated)*
Auxiliary atmospheric data	*ïOzone amount* *ïMeteorological profiles (7 levels + surface)*

Table 3. POLDER level 3 "ERB & clouds" product provided for each month

(1) AT THE GLOBAL SCALE :

PARAMETER	***Description***
BIDIRECTIONAL REFLECTANCE DISTRIBUTION FUNCTIONS	*ïNumber of observations, mean reflectance and standard deviation, mean bidirectional function (reflectance / albedo) and standard deviation, for 12 scene types and 800 angular bins*
BIDIRECTIONAL POLARIZATION DISTRIBUTION FUNCTIONS (only for ice clouds)	*ïNumber of observations, mean polarized reflectance and standard deviation, in 36 angular bins*

(2) AT THE SUPER-PIXEL SCALE :

PARAMETER	***Description***
General informations	*ïNumber of days N_{days}, number of orbits N_{orb}, etc.*
ALBEDOES at 443, 670, 865 nm and SW estimate	*ïMonthly mean and standard deviation* *ïMean of the clear-sky estimates*
CLOUD COVER	*ïMonthly mean and standard deviation* *ïMonthly mean uncertainty* *ïOccurence (number of days) in 10 classes*
WATER VAPOR CONTENT (only for clear-sky conditions)	*ïMonthly mean and standard deviation* *ï Occurence (number of days) in 10 classes*
CLOUD OPTICAL THICKNESS (simple linear average and energy-weighted average) O_2-APPARENT PRESSURE O_2-CLOUD PRESSURE RAYLEIGH-CLOUD PRESSURE	*ïMonthly mean and standard deviation* *ïDistribution (percentage of pixels) in 42 optical thickness / pressure classes* *ïOccurence (number of days) in 42 optical thickness / pressure classes*
CLOUD PHASE	*ïDistribution (percentage of pixels) in 5 classes* *ïOccurence (number of days) in 5 classes*

Table 4. Some characteristics of the observations reported in figure 2

EUCREX Flight number /POLDER Scene number	Day	Aircraft altitude (m)	Observed Cloudiness	Sea-surface wind speed ($m\ s^{-1}$)	Solar zenith angle
206 / 955	4/18/94	6090	Clear-sky	7	40°
206 / 820	4/18/94	6090	Stratocumulus	7	40°
205 / 713	4/17/94	10670	Cirrus	8.5	38°

Table A-1. Typical values of gaseous absorption in the POLDER channels used in the "ERB & clouds" line. These values correspond to a twofold path through the U.S.standard atmosphere (COESA 1976), with an air-mass factor of 3.

Channel	Ozone absorption (%)	Oxygen absorption (%)	Water vapor absorption (%)
443 nm	0.3	0	0.0
670 nm	4.5	0	1.5
763 nm (narrow)	0.6	41.6	1.4
765 nm (wide)	0.6	12.4	2.2
865 nm	0.0	0	2.7
910 nm	0.0	0	31.1

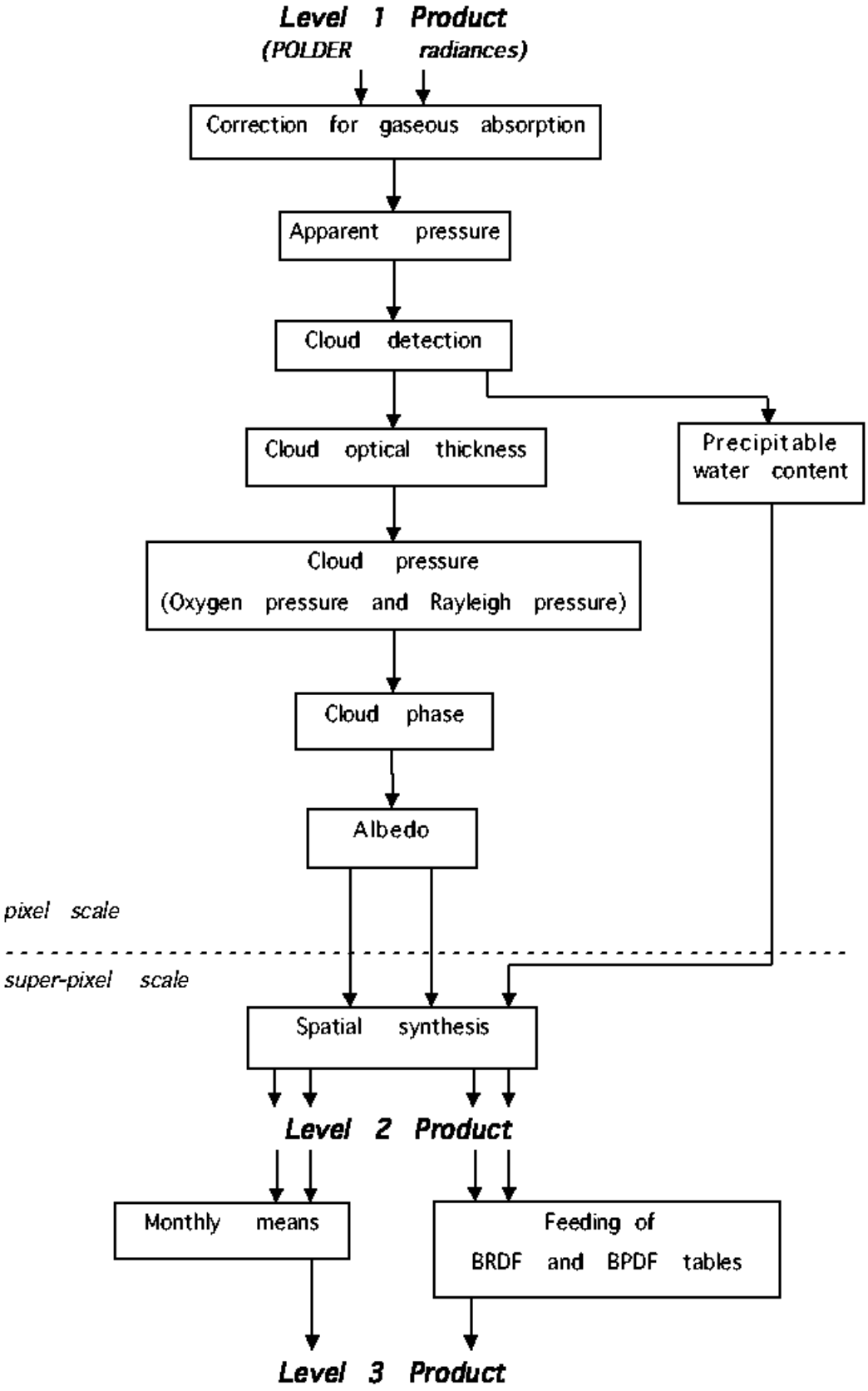

Figure 1 : Flow chart of POLDER data processing in the "ERB & clouds" line.

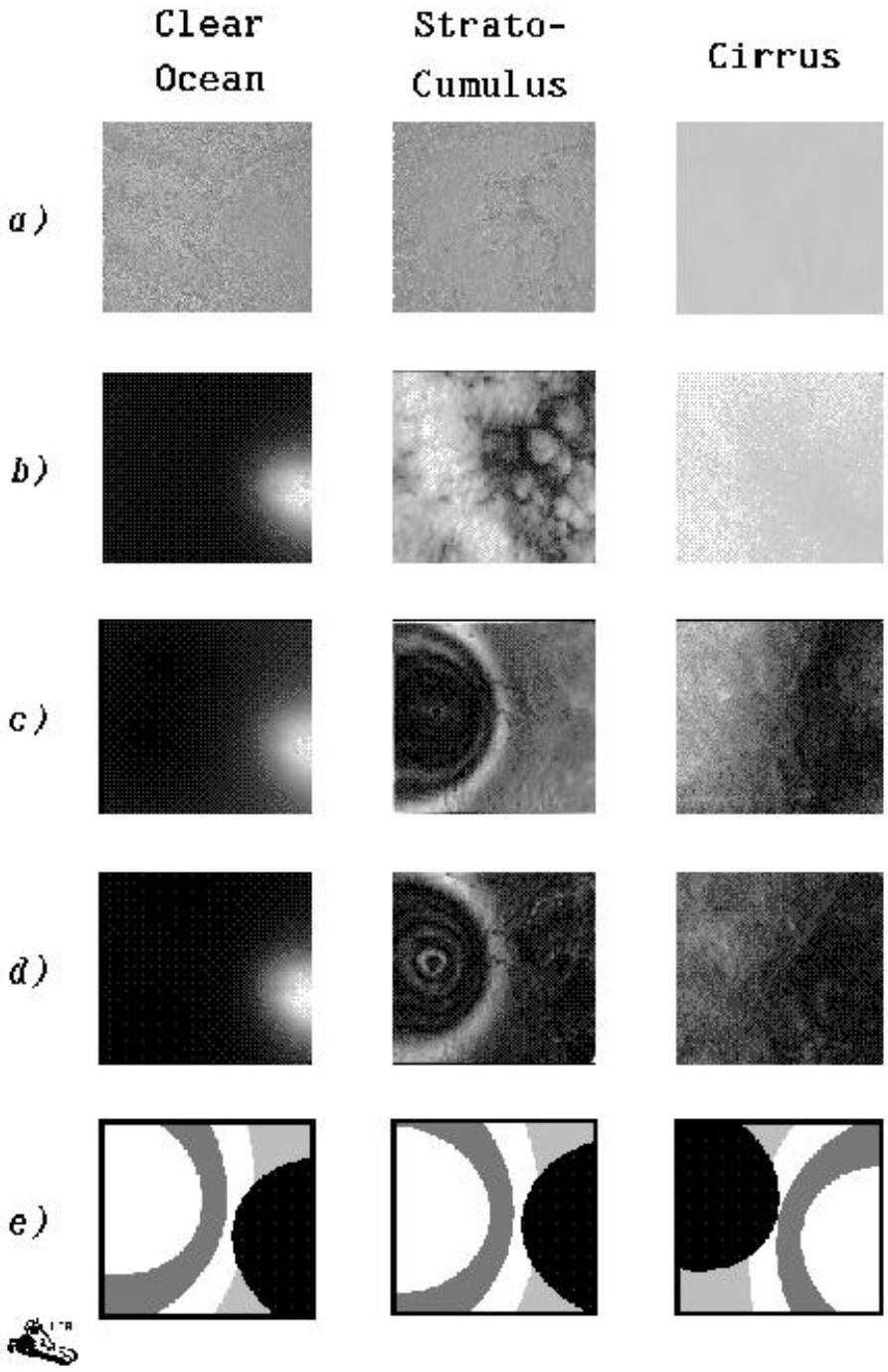

Figure 2 : Typical airborne POLDER measurements acquired during EUCREX'94 over clear ocean, stratocumulus and cirrus respectively. From top to bottom, are reported : (a) the ratio of reflectances measured in the narrow and the wide channels centered at 763 and 765 nm, (b) the reflectance measured at 865 nm, (c) the polarized reflectance

measured at 443 nm, (d) the polarized reflectance measured at 865 nm, and (e) some information about viewing directions, that is the expected region of the solar specular reflection (black), the expected cloud-bow region (dark grey) and the expected region of maximum molecular polarization (light grey).

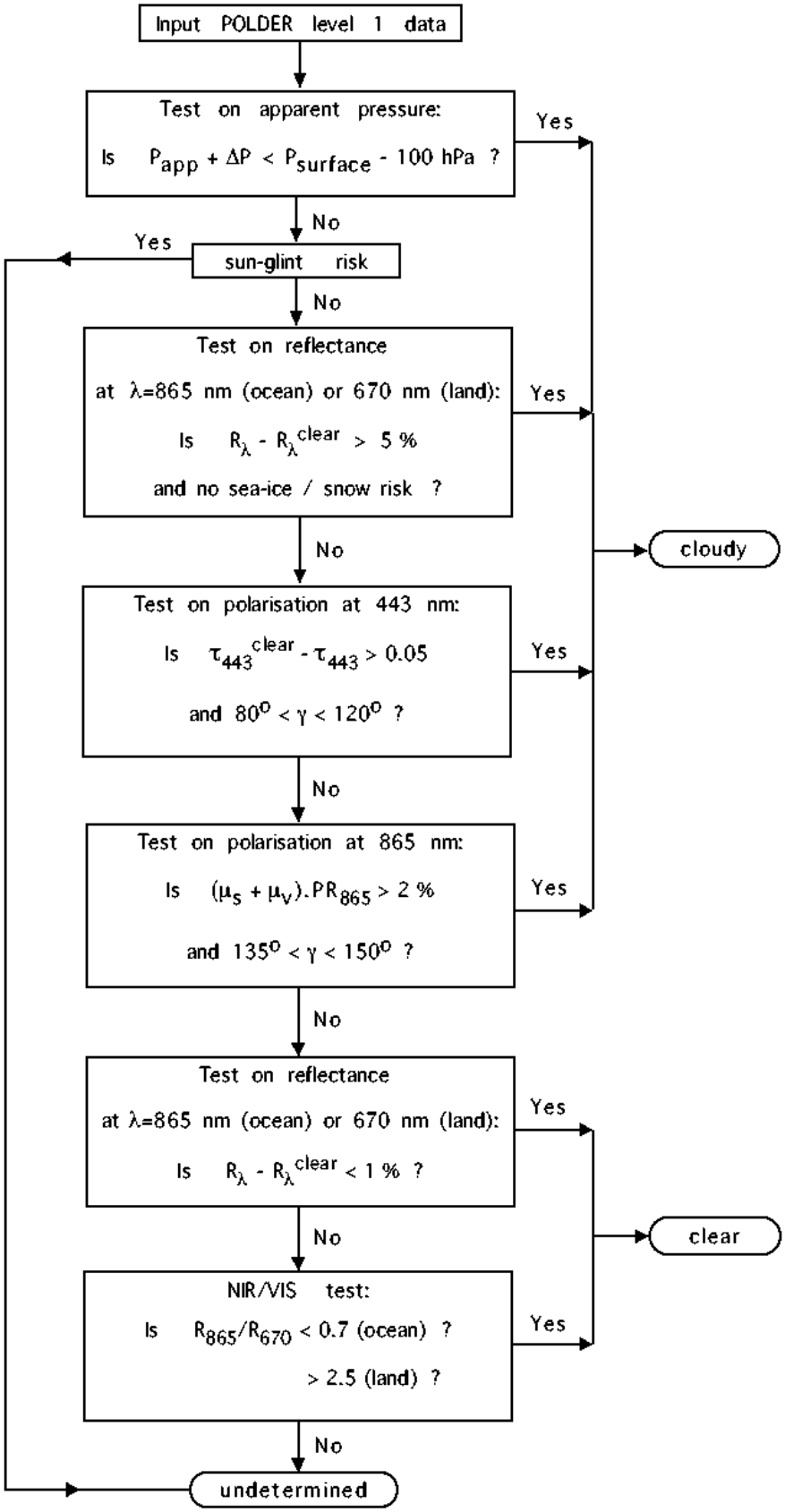

Figure 3 : Outline of the part of the cloud detection algorithm applied to each pixel and for every direction. The threshold values are only indicative.

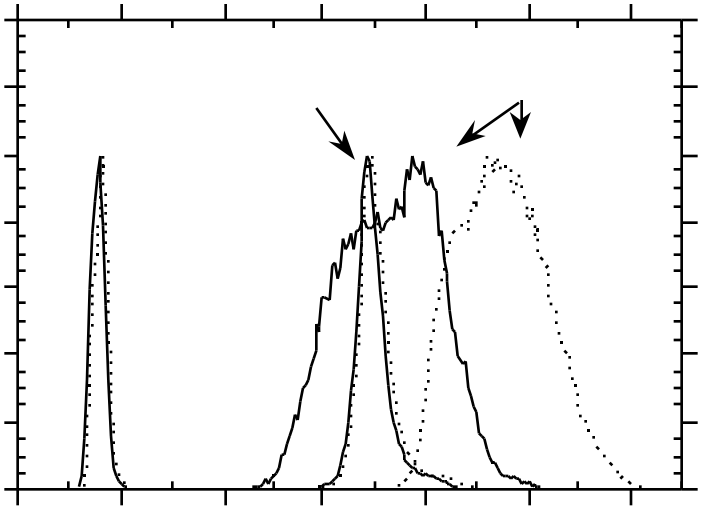

Figure 4 : Histogram of the apparent pressure P_{app} for the three scenes of figure 2 (solid lines). Are also reported the histograms of $P_{app} + \Delta P$ (dashed). See text for explanations.

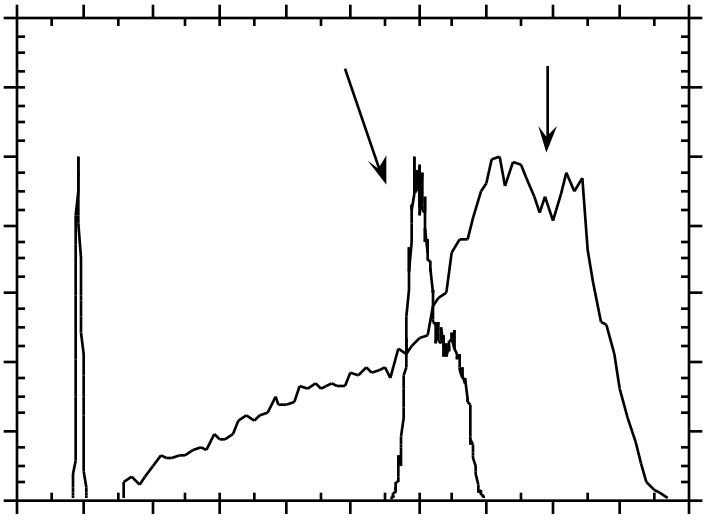

Figure 5 : Histogram of the difference between the measured reflectance at 865 nm and its clear-sky estimate (outside the sunglint zone), for the three scenes of figure†2.

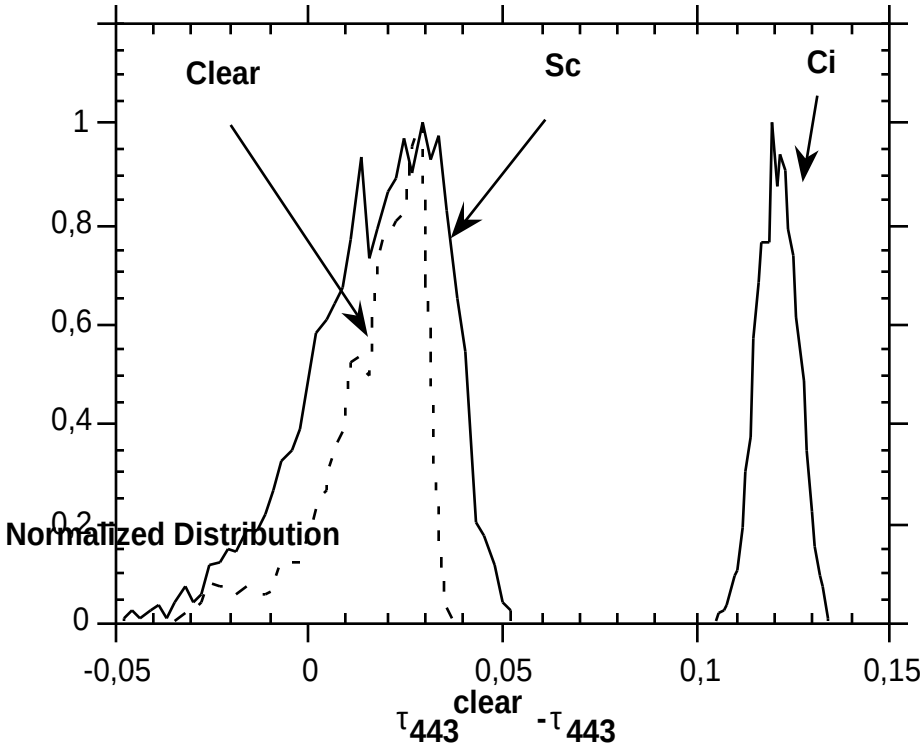

Figure 6 : Histogram of the difference between the molecular optical thickness of the atmosphere above the sea-surface and the estimate of the molecular optical thickness above the observed surface (ocean or cloud) from polarization at 443 nm, for the three scenes of figure 2. It is restricted to the region of maximum molecular scattering polarization ($80^o < \gamma < 120^o$) and outside the sunglint area.

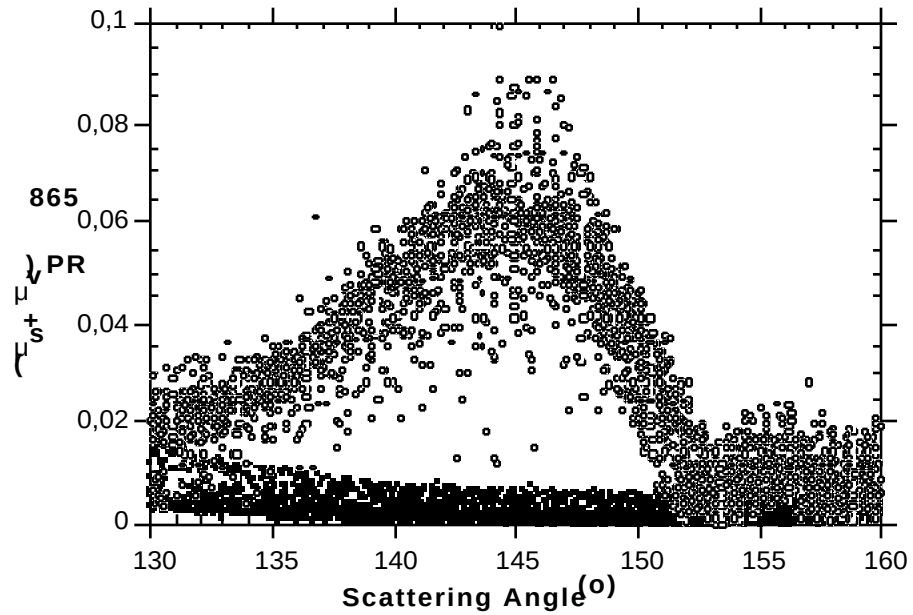

Figure 7 : Polarized reflectance at 865 nm weighted by (μ_S + μ_V) versus scattering angle for the stratocumulus cloud (open squares) and for the clear ocean (solid circles). μ_S and μ_V are the cosine of the solar and the satellite zenith angle respectively.

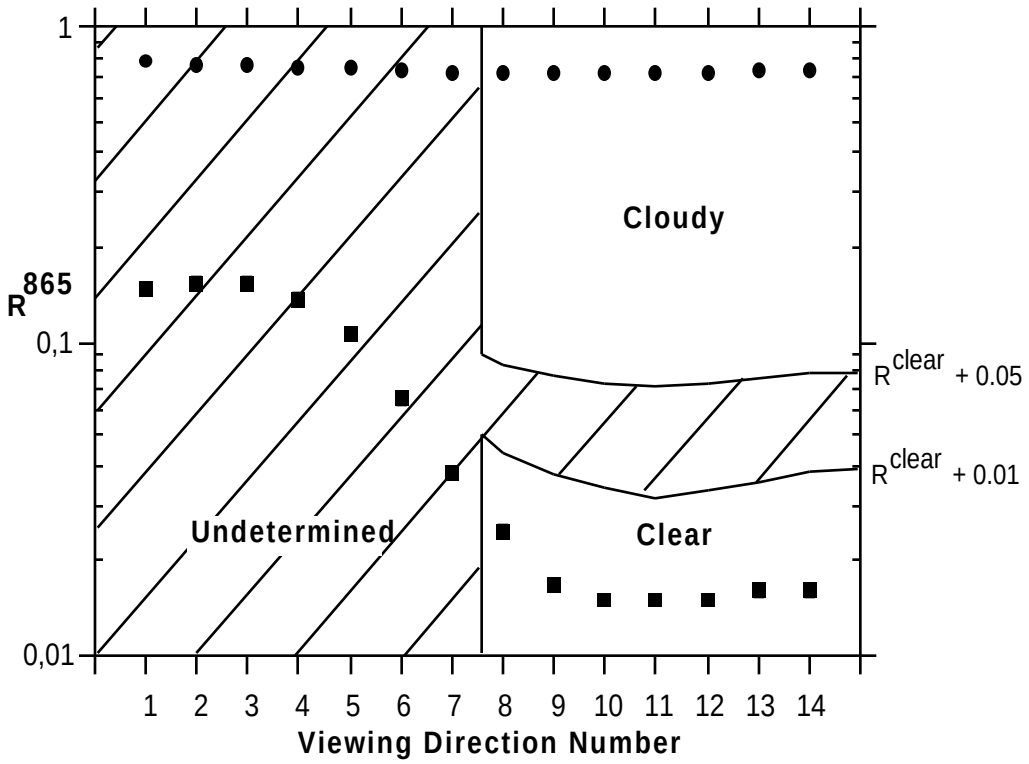

Figure 8 : Example of the 865 nm reflectance versus the viewing direction number, for a pixel of the stratocumulus scene (dots) and for a pixel of the clear-ocean scene (squares). The reflectance tests described in section 3.4 do not work in the expected sun-glint region (here, direction numbers 1 to 7) nor when the difference between the measured reflectance and its clear sky estimate is between 0.01 and 0.05. In the multi-direction test, a pixel that is labeled undetermined in some direction is re-labeled cloudy (or clear) for this direction if it has been declared cloudy (or clear) in the others directions.

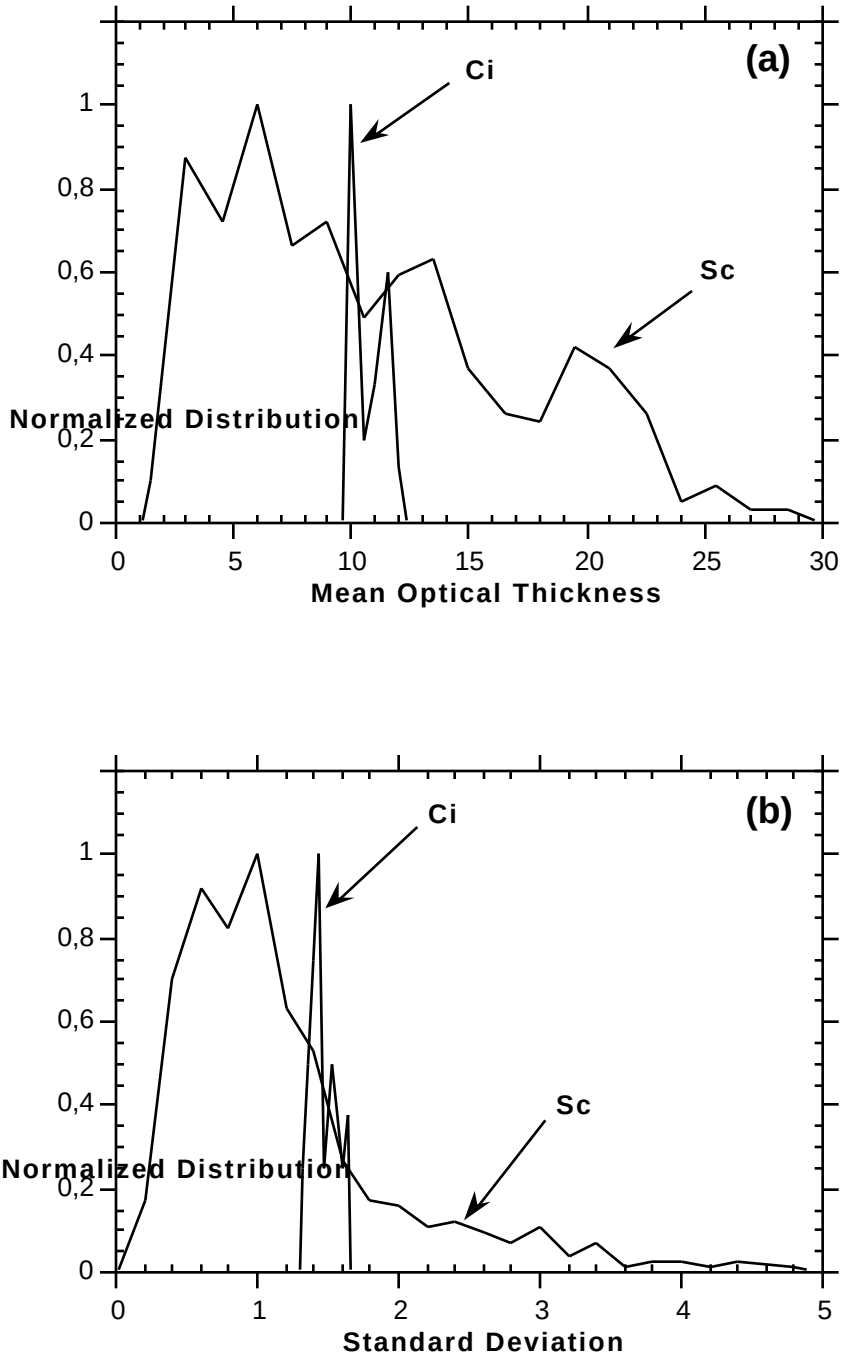

Figure 9 : Histogram of the mean of the 14 retrieved cloud optical thickness values (a) and of the standard deviation (b), for the stratocumulus and the cirrus pixels of figure 2.

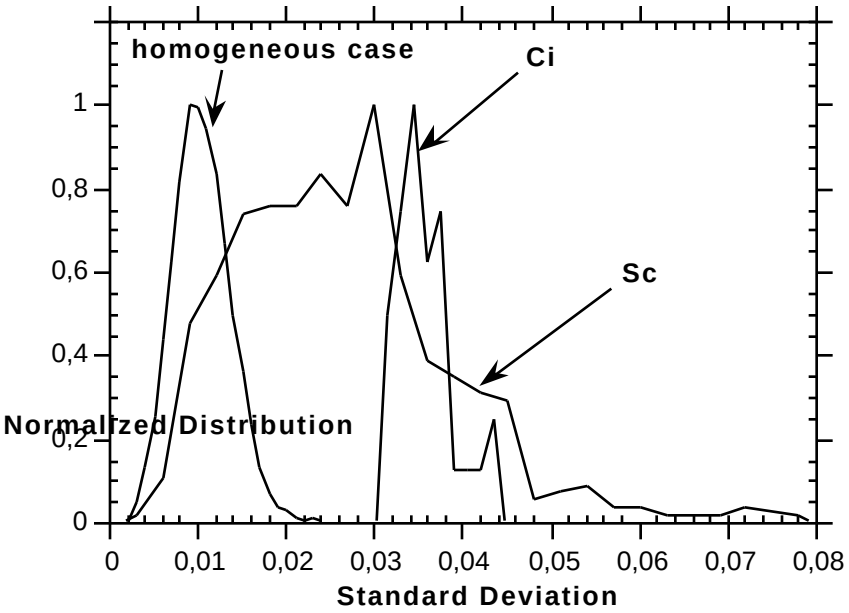

Figure 10 : Histogram of the standard deviation of the 14 retrieved albedo values for the stratocumulus and the cirrus pixels of figure 2. Also is reported the histogram corresponding to a "homogeneous" stratocumulus deck.

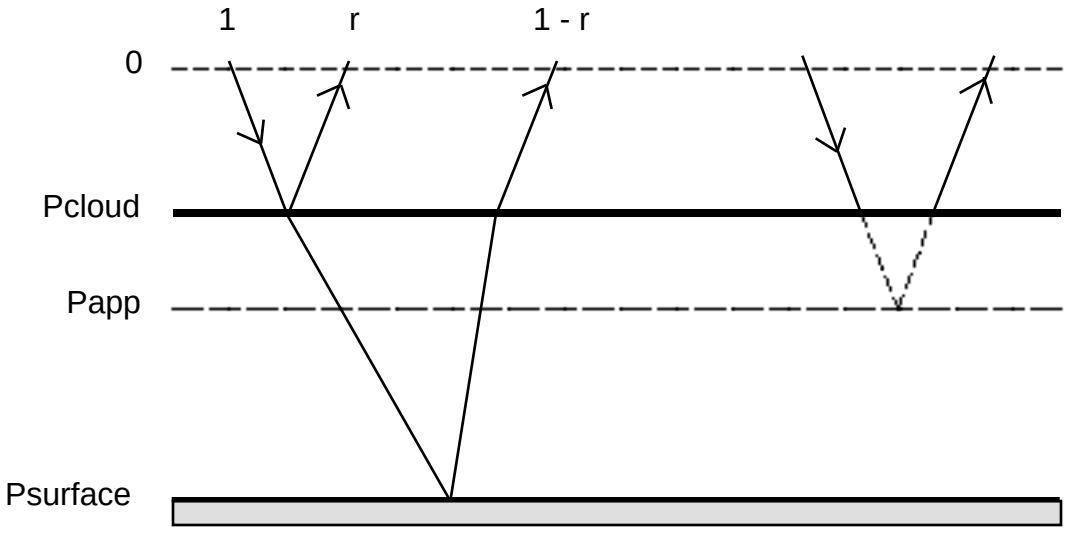

Figure 11 : Schematic representation of radiation transfer through a cloudy atmosphere. r is the percentage of photons directly reflected by the cloud.

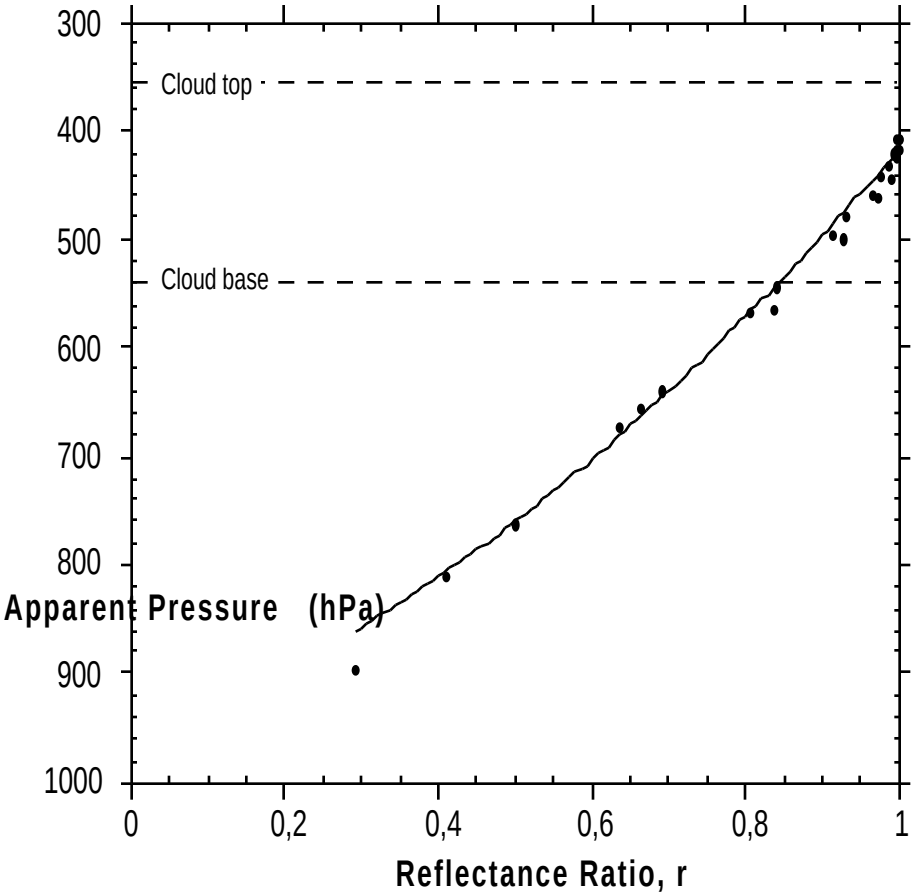

Figure 12 : Apparent pressure as a function of the ratio between the 763 nm reflectances calculated without and with the surface influence. The symbols correspond to values calculated by solving the radiative transfer equation for various surface reflectances and various cloud optical thicknesses. The simulation looks like the cirrus case shown on figure 2. The cloud top and cloud base pressure are 360 hPa and 540 hPa respectively. The air-mass factor *m* is equal to 3.3. The solid line corresponds to our approximation; it was obtained with equation (5), by using for P_{cloud} the value calculated for a black surface. This value of P_{cloud} varies from 410 to 510 hPa depending on the cloud optical thickness.

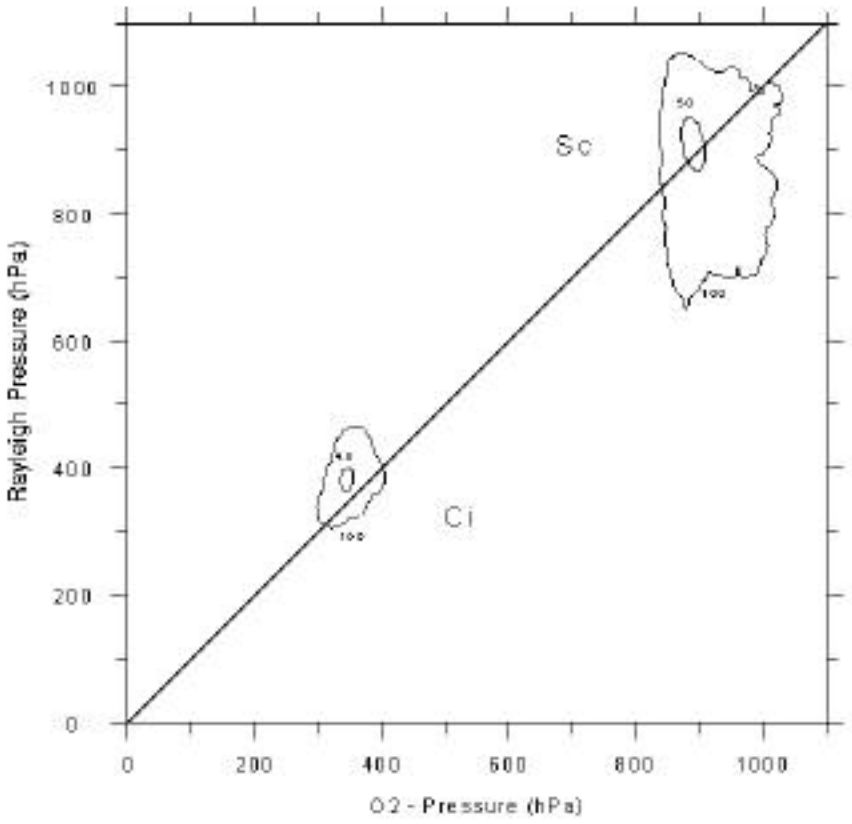

Figure 13 : Cloud pressure derived from polarization at 443 nm versus O_2-derived cloud pressure for the stratocumulus and the cirrus cloud (scattering angle between 80^o and 120^o, outside the sunglint zone). For each case, 50 percent of the pixels are situated within the isoline 50.

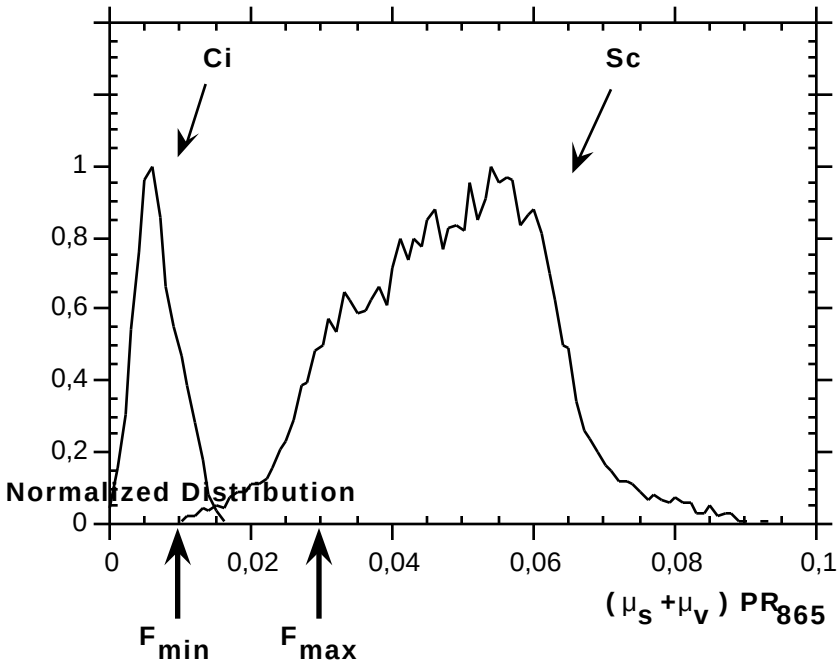

Figure 14 : Histogram of the weighted polarized reflectance at 865 nm $(\mu_s + \mu_v)\, PR_{865}$ for the stratocumulus and the cirrus cloud. It is restricted to the cloud-bow region (scattering angle between 135^o and 150^o), outside the sunglint zone. Cloud phase is assumed to be liquid or ice when $(\mu_s + \mu_v)\, PR_{865}$ is respectively larger than F_{max} or weaker than F_{min}.

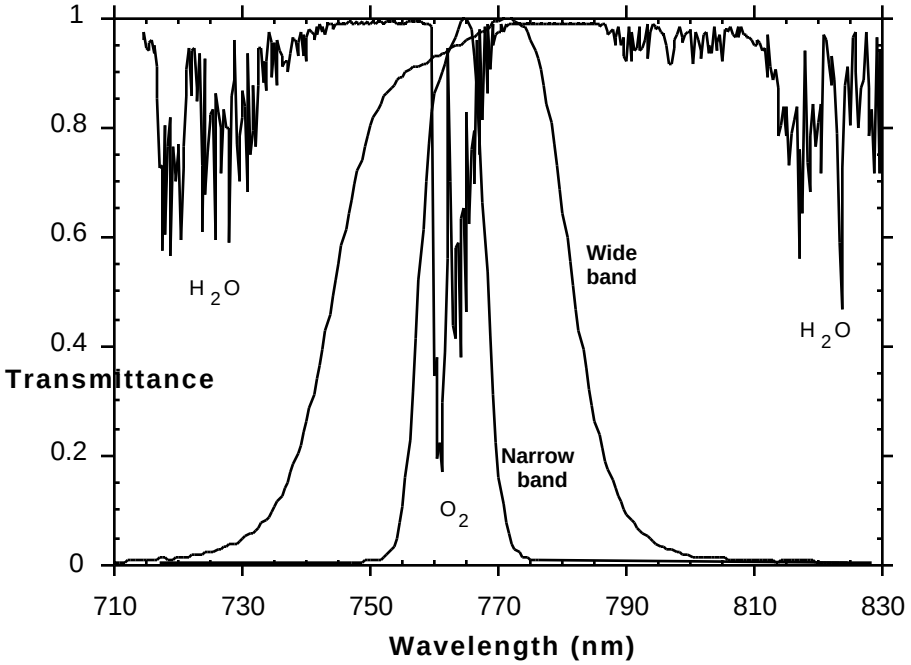

Figure A1 : Atmospheric transmission in the oxygen A-band region and filter transmissions in the narrow and wide bands centered at 763 nm and 765 nm respectively.